A&A 403, 119–134 (2003)
DOI: 10.1051/0004-6361:20030368

Astronomy & Astrophysics

Spatially–resolved spectrophotometric analysis and modelling of the Superantennae⋆

S. Berta[1], J. Fritz[1], A. Franceschini[1], A. Bressan[2], and C. Pernechele[2]

[1] Dipartimento di Astronomia, vicolo dell'Osservatorio 2, 35122 Padova, Italy
[2] Osservatorio Astronomico di Padova, vicolo dell'Osservatorio 5, 35122 Padova, Italy

Received 8 August 2002 / Accepted 11 March 2003

Abstract. We have performed spatially–resolved spectroscopy of the double–nucleated Ultra-Luminous Infrared Galaxy IRAS 19254–7245, "the Superantennae", along the line connecting the two nuclei. These data are analysed with a spectral synthesis code, to derive the star formation and extinction properties of the galaxy. The star formation history (SFH) of the two nuclei is similarly characterized by two different main episodes: a recent burst, responsible of the observed emission lines, and an older one, occurred roughly 1 Gyr ago. We tentatively associate this bimodal SFH with a double encounter in the dynamical history of the merger. We have complemented our study with a detailed analysis of the broad band spectral energy distribution of the Superantennae, built from published photometry, providing the separate optical-to-mm SEDs of the two nuclei. Our analysis shows that: a) the southern nucleus is responsible for about 80% of the total infrared luminosity of the system, b) the L-band luminosity in the southern nucleus is dominated by the emission from an obscured AGN, providing about 40 to 50% of the bolometric flux between 8 and 1000 μm; c) the northern nucleus does not show evidence for AGN emission and appears to be in a post–starburst phase. As for the relative strengths of the AGN and starburst components, we find that, while they are comparable at FIR and sub–mm wavelengths, in the radio the Sy2 emission dominates by an order of magnitude the starburst.

Key words. galaxies: individual: IRAS 19254-7245 –galaxies: interactions – galaxies: starburst – galaxies: Seyfert

1. Introduction

Starburst galaxies are characterized by a substantially enhanced ongoing star formation with respect to their past average. Though initially selected as having intense optical emission lines, it has later become clear that the main phases of star formation are highly attenuated in the optical and luminous in the infrared (the IRAS-discovered Luminous and Ultra-Luminous Infrared Galaxies – LIRGs and ULIRGs). The Infrared Space Observatory (ISO), together with ground-based mm facilities such as SCUBA on the JCMT, showed the existence of distant galaxies with enhanced IR emission (e.g. Elbaz et al. 1999; Barger et al. 2000; Smail et al. 2000; Franceschini et al. 2001), characterized by a strong cosmological evolution, and partly responsible for the cosmic IR background (Puget et al. 1996; Hauser at al. 1998). This high-redshift population of relatively unfrequent but very luminous galaxies constitute a new important cosmological component.

With luminosities in the range 10^{11}–10^{13} $L_{\odot}$ and space densities similar to those of quasars (Soifer et al. 1986), the ULIRGs are the most powerful objects in the nearby Universe (Sanders & Mirabel 1996) and are considered to be the local counterparts of the newly discovered high-z IR luminous galaxies. Understanding the nature of such ultra-luminous sources is then an important task for observational cosmology, as they may correspond to the phases of formation, or the assembly, of spheroidal galaxies.

Local infrared galaxies show evidence, from the optical emission lines, that their high luminosities are due to dust reprocessing of the light emitted by young massive stars. However, the small sizes of the nuclear star forming regions of compact ULIRGs are also consistent with a significant fraction of their IR emission being provided by an AGN (Soifer et al. 2000). The fact that in such objects the star formation rate (SFR) deduced from the IR luminosity often exceeds that derived from the extinction-corrected optical line intensities (Poggianti et al. 2001) has been taken as an indication for an obscured AGN contribution. A concomitant starburst- and AGN-activity is sometimes clearly revealed by broad optical and high excitation lines.

Whether this double–nature phenomenon is occasional or starburst activity is systematically accompanied by an AGN, is still a matter of debate. The existence of a massive dark objects in the nuclei of galaxy spheroids (Magorrian et al. 1998;

Send offprint requests to: S. Berta,
e-mail: berta@pd.astro.it

⋆ Based on observations collected at the European Southern Observatory, Chile, ESO No. 66.B-0706.

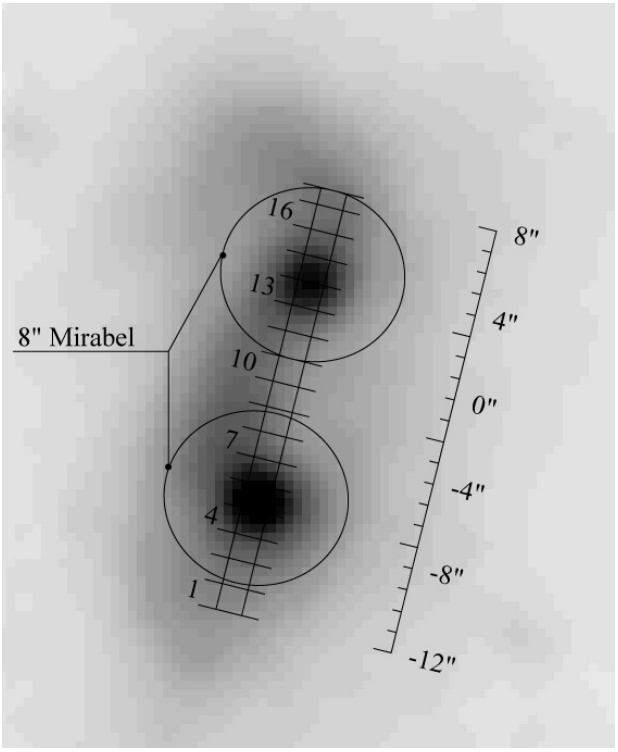

Fig. 1. Position of the central slitlet on the *B* image taken at the 3.6 m ESO telescope. The spatial spectral analysis has been obtained by cutting the slit region in 17 slices, as numbered in the figure. The two circular apertures centerd on each nuclei and with a diameter of 8 arcsecs correspond to those adopted by Mirabel et al. (1991). See text for more details.

Merritt & Ferrarese 2001) may indeed suggest that the AGN activity should have been a widespread phenomenon, at least in the past.

With the aim of further investigating the nature of luminous IR galaxies, we performed a spatially–resolved spectropolarimetric study of a small sample of ULIRGs selected from the Genzel et al. (1998) mid–IR sample of 15 ULIRGs, based on a complete IRAS sample with $S_{60\ \mu\mathrm{m}} \geq 5.4$ Jy (Pernechele et al. 2003). The far–infrared selection ensures minimal bias by dust absorption. In this way we aim at identifying signatures in the SEDs of these sources which can be used to estimate the AGN contribution; the mechanisms quenching out the central AGN after the dynamical destabilization of the gas; the relationship between the star formation process and the dynamical interaction.

In this paper we analyse the full-light spectrum of an ULIRG prototype whose nature (staburst/AGN) is still intriguing: the Superantennae (IRAS 19254–7245). At a redshift $z = 0.061709$ (Strauss et al. 1992) and with a total infrared luminosity of about $1.4 \times 10^{12}\ L_{\odot}$ (we use $H_0 = 65$ [km s^{-1} Mpc^{-1}]), the Superantennae represents one of the most powerful galaxy collisions in the nearby universe, exhibiting two giant tails extending 350 kpc away from two nuclei, separated by ∼10 arcsec. This galaxy has been already studied by Mirabel et al. (1991) and Colina et al. (1991), who report evidence of a type-2 AGN with a biconical galactic wind up to 800 km s^{-1}.

The paper is structured as follows. In Sect. 2 we describe the observations and data reduction. Section 3 is devoted to the analysis of the most relevant characteristics of the spatially–resolved spectra and of some physical properties, such as extinction and star formation rate. In Sect. 4 we build a consistent broad band spectral energy distribution of the two nuclei. These allow us to evaluate in Sect. 6 the contribution of the star formation process and the AGN to the bolometric infrared emission. The optical spectrum of the two nuclei, corrected for the contribution of the AGN, is thus analyzed by means of a population synthesis tool described in Sect. 5, the results are presented in Sect. 7. Section 8 is devoted to the discussion of the star formation history and the AGN non-thermal component of Superantennae. Section 9 contains our conclusions. We adopt $H_0 = 65$ [km s^{-1} Mpc^{-1}].

2. Observations and data reduction

The spectropolarimetric observations of the Superantennae were done with EFOSC2 at the 3.6 m ESO telescope in La Silla, during the night of November the 1st, 2000. The seeing was about 1 arcsec and some veils were present at low sky altitude. For this reason particular care has been taken in observing the target at its maximum elevation and chosing the standard star close to the object, in order to perform absolute flux calibration. We notice in advance that, once properly corrected for aperture losses, the calibrated spectra consistently fit the available literature optical and near–IR photometry (see Sect. 6).

Polarimetric observations were obtained adopting a rotating $\lambda/2$ retarder plate and a Wollastone prism, inserted before the grism. We choose the 236 lines mm^{-1} grism, with a dispersion of 2.77 Å pixel^{-1}, covering the 3685–9315 Å wavelength range and a 1.2×20 arcsec slit, corresponding to a spectral resolution of 21.2 Å. The slit was oriented with a PA of 14°, such that both Superantennae's nuclei were included.

The data consist in a set of four couples of frames, obtained with retarder–plate angles of 0, 22.5, 45 and 67.5 degrees, for a total integration time of 6000 s. Johnson *B* and *R* band images were also obtained, with exposure times of 900 and 480 s, respectively.

The data reduction has been carried out with the use of IRAF's standard tasks and IDL procedures developed by ourselves.

Polarimetry is reported by Pernechele et al. (2003), while here we analyze the full-light spatially-resolved spectrum.

The Wollastone prism splits the light into two perpendicularly polarized beams, which are projected onto the CCD. To avoid overlapping, the slit is transparent only in a series of 5 slots, separated by 5 opaque masks. The prism causes each frame to appear as composed of 5 couples of spectra (hereafter "strips"), belonging to the 5 different slots.

The frames were bias and flat–field corrected in the usual way. Then the two strips including the object's traces and two sky–strips were cropped. Each strip was flux calibrated with the spectrophotometric standard star in the centre of NGC 7293 (Oke 1990) and then sky-subtracted. Unfortunately, the interposition of the prism between the retarder plate and the grism

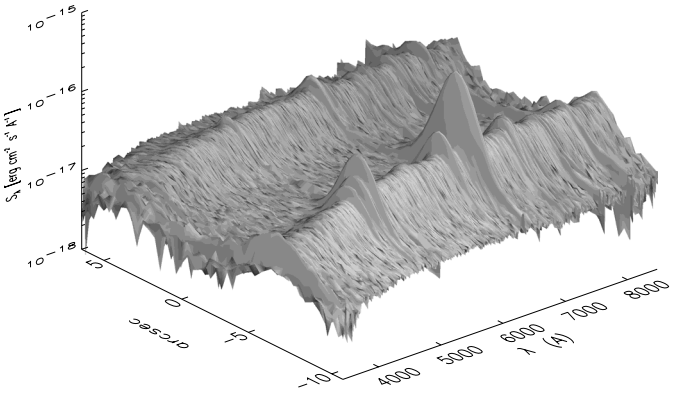

Fig. 2. The three–dimensional structure of the spectrum obtained with the pipeline described in Sect. 2. Different emission lines are already clearly visible, Hα standing over all the others. The spatial axis corresponds to the one shown in Fig. 1.

induces strong distortions of the frames, so we needed to provide a distortion map by means of a polynomial fit using IDL. Each spectrum was corrected for galactic reddening, assuming $R_V = 3.1$ and $E(B-V) = 0.086$ (Schlegel et al. 1998) and finally the various strips, relative to 4 different polarization angles, were combined together to produce the spatially resolved total-light spectrum of Fig. 2.

The spectra of the nuclei were simply extracted through apertures of 1.2×3.6 arcsec^2 (for the southern) and 1.2×2.4 arcsec^2 (for the northern nucleus), see Fig. 3. At a redshift $z = 0.06171$, 1 arcsec corresponds to ∼1.4 kpc.

3. Analysis of the spatial dependence of the most relevant spectral features

The high quality total–light spectrum allowed us to perform an analysis of the main spectral features of Superantennae along the whole slit, hence to probe the spatial dependence of some physical properties along the line connecting the two nuclei.

To take into account the effects of the poor seeing, we binned our spectrum in steps of 3 pixels along the spatial axis (corresponding to 1.2 arcsec) and thus obtained seventeen independent spectra corresponding to different regions of the galaxy. In Fig. 1 the 1.2″ slit has been superposed on the *B* band image taken with EFOSC2: the different spectra obtained with the binning procedure correspond to the regions numbered from 1 to 17 in the figure. This also indicates the 8″ apertures used by Mirabel et al. (1991) in their photometric study of the Superantennae (which we will use in the following to estimate the contribution of the two nuclei to the total infrared flux).

3.1. Emission lines

The 17 spectra corresponding to the different regions along the slit (Fig. 1) are shown in Fig. 4. Several optical emission lines typical of starburst galaxies can be recognized (see also Fig. 3): [OII](3727 Å), Hβ(4861 Å), the sum of the two [OIII](4959 and 5007 Å), [OI](6300 Å), the blend of Hα (6563 Å) and the two [NII]'s (6548 and 6584 Å), and the blend of [SII] (6717 and 6731 Å).

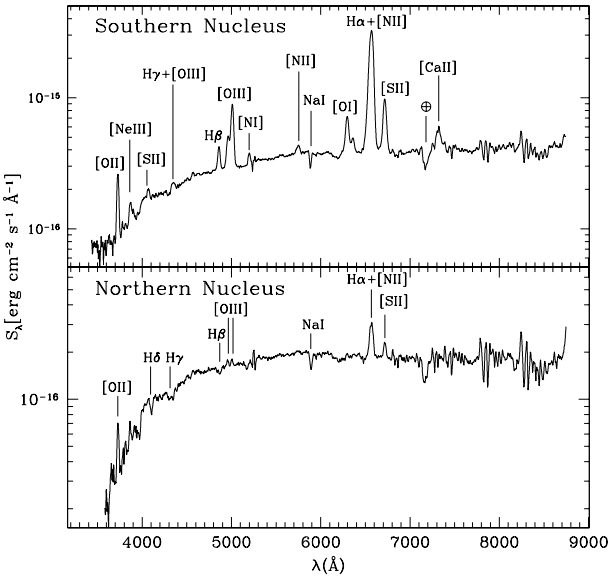

Fig. 3. The spectra of the two nuclei of IRAS 19254-7245 as extracted from an aperture of $1.2'' \times 3.6''$ for the southern nucleus, and $1.2'' \times 2.4''$ for the northern, respectively. A lot of emission lines typical of ULIRGs are recognizable.

The corresponding line fluxes are reported in Table 1. Figure 5 compares the profiles of the various line fluxes (solid line) along the spatial direction with the intensity of the continuum between 5500 and 5600 Å (dotted line) normalized to the line intensity peak value. It turns out that, with the exception of the [OII] (see Fritz et al. 2002, for a discussion), all other emission lines are much more peaked than the continuum, indicating that the ongoing star formation or the AGN activity is strongly concentrated within the nuclei.

The southern nucleus shows both narrow permitted and forbidden lines; we don't have enough spectral resolution to separate Hα (6563 Å) from the two [NII]'s (6548 and 6584 Å), but Mirabel et al. (1991) reports that [NII] is stronger and sharper than Hα, thus revealing the Seyfert 2 nature of this emission.

For the same reason we cannot discriminate between [OIII]λ4363 and Hγ or [SII]λ6717 and [SII]λ6731 and, consequently, we cannot derive an estimate of the electron density. By adopting the value of $N_e = 670$ cm^{-3} provided by (Colina et al. 1991), we use the fluxes of [NII]λ5755 and [NII]$\lambda\lambda$6548+6583 to estimate the electron temperature in the southern nucleus (spectra #4, 5 and 6). [NII]λ5755 was deblended from [FeVII]λ5721, while the ratio between Hα and [NII]$\lambda\lambda$6548+6583 has been inferred from Colina et al. (1991) data as described next. The estimated electron temperature in the southern nucleus is $T_e \sim 14\,600$ K, consistent with the Colina et al. (1991) range of 10^4–2.5×10^4 K.

The northern nucleus is characterized by a much lower star formation activity, as it is evident from the lower intensity of the lines or even the prevalence of photospheric absorption for Hβ and Hγ. A detailed analysis reveals that the [OIII]λ4363 + Hγ blend is in emission in the three central spectra of the southern nucleus, possibly because of a strong forbidden oxygen emission in the Seyfert component, but then moving outwards and to the northern nucleus it switches to

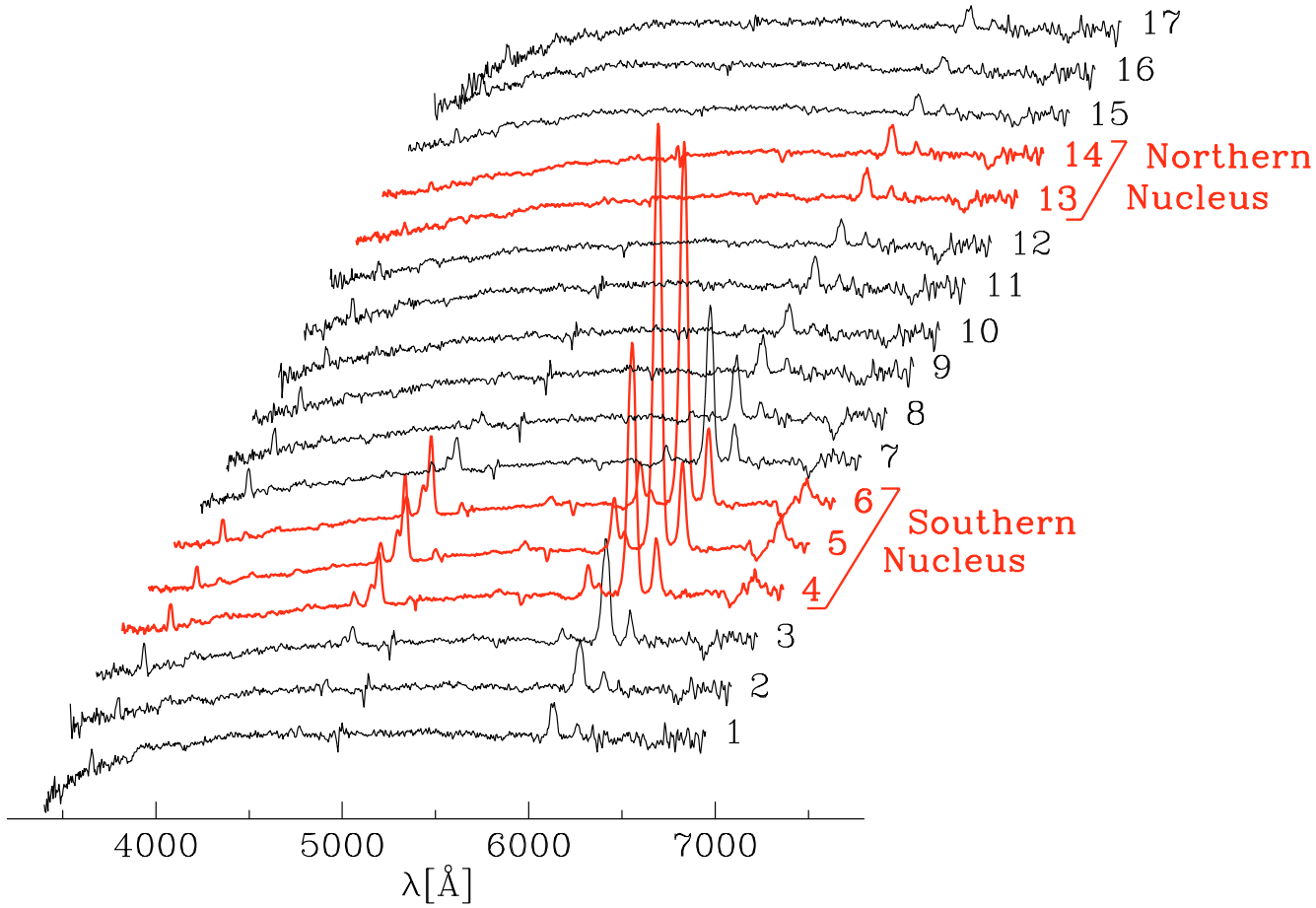

Fig. 4. The seventeen different slices of Fig. 1 are plotted in sequence, to show the trend of the continuum and other spectral features, as a function of position along the slit.

absorption, dominated by photospheric Hγ. Also the blue edge of the continuum steepens significantly towards the northern component, showing that this nucleus is dominated by an older stellar population.

3.1.1. Extinction from the line ratios

The comparison of the observed Hα/Hβ ratio with the theoretical value of 2.85 predicted for a Case–B recombination (Osterbrock 1989), allows in principle to derive the average extinction, at least for the southern nucleus where Hβ is detected in emission. To this end, we first need to quantify the contribution of the two [NII] lines at 6548 and 6584 Å to the Hα+[NII] blend, because the Seyfert 2 nature of this nucleus prevents from adopting standard starburst values for the line ratio. From the high resolution spectrum of Colina et al. (1991), we know that in the southern nucleus $S(\mathrm{H}\alpha) = \frac{3}{4}S([\mathrm{NII}](6584))$, hence assuming for the ratio between the two [NII] the standard value ($\frac{1}{3}$), we get:

$$S(\mathrm{H}\alpha) = \frac{9}{25}S(\mathrm{blend}). \quad (1)$$

Similarly, in the northern nucleus we obtain (Colina et al. 1991) $S(\mathrm{H}\alpha) \simeq \frac{1}{2}S(\mathrm{blend})$.

Since Colina et al. (1991) spectra of the two nuclei were obtained through a $3'' \times 6''$ aperture, in the following we adopt Eq. (1) on spectra #2 to #8, centered on the Southern nucleus and the more standard value of $\frac{1}{2}$ in the Northern nucleus and outer regions of the Superantennae.

To compare the empirical extinction estimate with the model prediction (see Sect. 8) we need to further correct the observed Hβ flux for the photospheric stellar absorption. On this subject González Delgado et al. (1999) found that the contribution to the Hβ equivalent width from intermediate–age stars in starburst galaxies is 2–5 Å. Since they do not account for an old disc population, which would decrease these values, we have adopted a mean absorbing equivalent width of 2 Å. The color excess $E(B-V)$, derived from the Hα/Hβ ratio is reported in the last column of Table 1. We plot in Fig. 6 the spatial dependence of the $E(B-V)$ (upper panel) and of Hα (middle panel) and Hβ line intensities.

The values of $E(B-V) \sim 1.0$ mag in the central regions obtained in this way are smaller than the value of $E(B-V) \simeq 1.4$ mag reported by Colina et al. (1991), but are consistent with those obtained by our more detailed spectral analysis discussed in Sect. 5, which considers the presence of an old population. Also Vanzi et al. (2002) find $A_V = 3.15$, consistent with our result. This technique cannot be applied in the outer regions of the system and in the northern nucleus, where Hβ is either not detected or in absorption. In those regions, spectral synthesis models (see Fig. 16) yield a mean value of $E(B-V) \sim 0.4$–0.5,

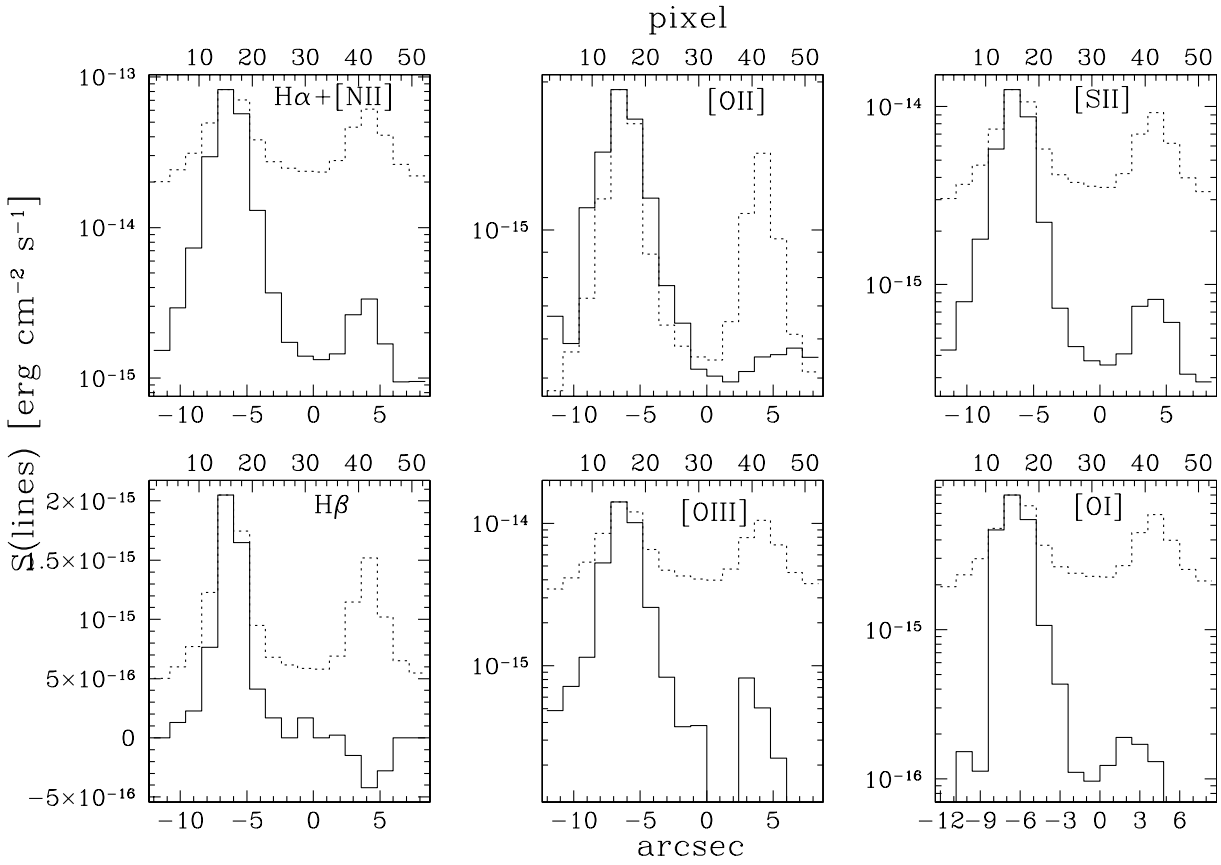

Fig. 5. Spatial profile of the main emission lines. The solid histograms represent the profiles of the various lines, as indicated in the panels. To study the spatial profile of the lines, we plot the continuum normalized to the peak value of line emission in the sounthern nucleus (dotted histogram): going from the brightest nucleus to the outer regions, all the lines but [OII] fade more rapidly than the continuum.

consistent with the typical average colour excess ≃0.3 of spiral galaxies.

Hopkins et al. (2001) and Sullivan et al. (2001) notice the existence of a correlation between the extinction, derived from the Balmer decrement, and the intensity of the Hα emission line, in a sample of star forming galaxies. The same trend is clear in our spatially resolved analysis of Superantennae, when we plot the ratios of [OII](3727 Å) and Hβ to Hα, as a function of the Hα flux (Fig. 7). The observed ratio decreases as the Hα intensity increases, confirming a strong correlation between extinction and the star formation activity, as expected if the latter is a function of the local density of gas and dust, and if the extinction is mainly due to a foreground screen. The correlation involving [OII](3727 Å), see top panel in Fig. 7, seems to indicate that [OII] and Hα emissions are largely independent, in fact the [OII] strength only slightly depends on position along the slit. We defer to Fritz et al. (2003) for a more detailed discussion of this effect.

3.1.2. The star formation rate

In star forming galaxies the extinction-corrected Hα line intensity is a powerful tool to estimate the rate of ongoing star formation. Poggianti et al. (2001), however, have warned that for particularly extinguished objects the star formation rate determined in such way may be significantly underestimated, by values up to a factor 3 compared with those derived from the far infrared luminosity. Furthermore, as it will be discussed later, the Superantennae shows strong evidence of a significant AGN component, probably contributing also to optical emission lines.

With these caveats in mind, we have applied the relation of Kennicutt (1998) to the Hα emission corrected for the [NII] contribution to the blend, for extinction, and for the AGN contribution, to derive a preliminary estimate of the corresponding SFR, leaving a more accurate analysis to the following sections.

Kennicutt assumes a Salpeter IMF between 0.1 and 100 $M_\odot$, solar abundance and a constant star formation rate during 10^8 yr:

$$SFR(M_\odot \mathrm{yr}^{-1}) = 7.9 \times 10^{-42} L_{\mathrm{H}\alpha}\,(\mathrm{erg\,s}^{-1}). \quad (2)$$

The results are summarized in the first column of Table 4 (see Sect. 8), with values ranging between ∼47 $M_\odot$/yr in the southern nucleus and ∼0.4 $M_\odot$/yr in the northern.

4. The broad band spectral energy distribution

Further information on the source comes from the analysis of the broad band energy distribution. We have collected all the photometric data available on IRAS 19254–7245 with the purpose of obtaining a reliable spectral energy distribution for its two components.

Table 1. Flux intensities of the main emission lines detected, measured on the extracted spectra (no slit losses correction applied yet). The first column indicates the label of the spectrum as specified in Fig. 1. In the next eight columns we report the observed fluxes of [OII] (3727 Å), Hβ (4861 Å), [OIII] (4959 + 5007 Å), [OI] (6300 Å), Hα+[NII] (6563, 6548 and 6584 Å) and [SII] (6717 Å), respectively. Fluxes are in 10^{-16} [erg cm^{-2} s^{-1}]. The last column shows the $E(B-V)$ derived from the Balmer decrement, as described in the text. The last two rows report the fluxes for the two nuclei: the southern consists of spectra #4, 5 and 6, the northern of #13 and 14. The nuclear fluxes are larger than the sum of fluxes in individual spectra, because they were measured on total nuclei extractions and not computed as sums.

Spectrum	S([OII])	S(B)	S(Hβ)	S([OIII])	S(V)	S([OI])	S(Hα+[NII])	S([SII])	$E(B-V)$
1	6.68	0.28	–	2.01+2.84	0.36	–	15.3	4.28	–
2	5.88	0.34	1.28	2.47+4.69	0.43	1.53	29.3	8.03	0.429
3	11.1	0.41	2.28	3.32+8.16	0.55	4.97	72.9	18.0	0.730
4	14.4	0.57	7.65	16.1+36.7	0.88	25.8	295.	57.9	1.013
5	19.3	0.85	20.5	42.3+99.3	1.47	74.5	826.	125.	1.090
6	16.8	0.75	16.5	28.4+72.7	1.25	46.8	570.	87.8	0.974
7	11.6	0.43	4.10	7.10+18.5	0.68	7.13	130.	22.4	0.827
8	77.0	0.31	1.69	2.70+5.60	0.49	3.20	36.7	7.37	0.450
9	6.46	0.28	–	0.814+2.91	0.44	1.31	17.3	4.48	–
10	5.21	0.28	–	1.03+2.78	0.42	1.06	14.0	3.73	–
11	5.04	0.29	–	–	0.41	–	13.3	3.53	–
12	4.91	0.34	–	–	0.49	1.55	14.5	4.09	–
13	5.15	0.53	−1.50	3.70+4.51	0.82	1.75	26.3	7.54	–
14	5.52	0.66	−4.20	2.17+2.87	1.09	1.31	33.5	8.26	–
15	5.58	0.56	−2.80	0.885+1.36	0.73	–	16.9	6.12	–
16	5.75	0.42	–	–	0.47	–	9.44	3.13	–
17	5.51	0.30	–	–	0.39	–	9.52	2.84	–
South. Nucl.	48.8	2.16	43.9	84.8+208	3.59	156.	1680.	240.	1.042
North. Nucl.	9.26	1.19	−6.60	3.73+5.03	1.91	4.03	57.0	13.2	–

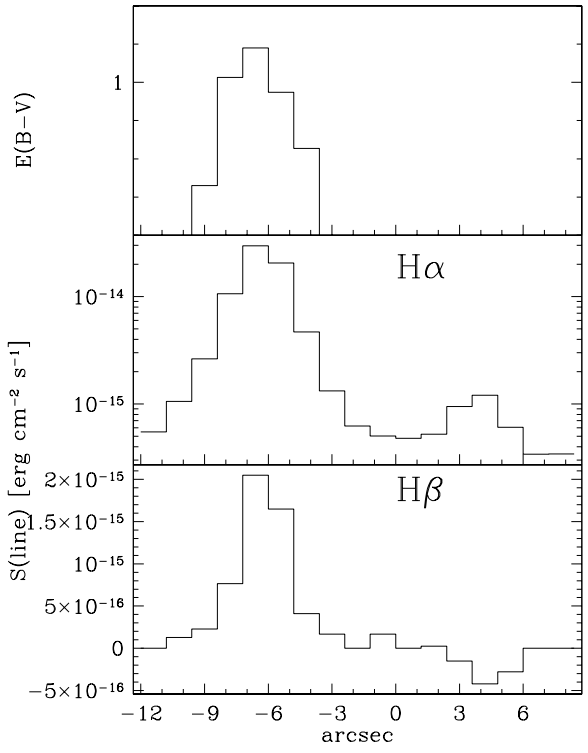

Fig. 6. Upper panel: spatial dependence of the extinction, $E(B-V)$, as computed from the Balmer decrement along the slit. Middle and lower panels: Hα and Hβ fluxes. The Hβ flux scale is linear instead of logarithmic because the line is seen in absorption in the Northern nucleus.

Mirabel et al. (1991) report magnitudes in the optical and near–IR, from the B up to the L and N bands, within 8″ apertures centered on the two nuclei, as well as the total corrected IRAS fluxes at 12, 25, 60 and 100 μm with uncertainties of 11%, 5%, 4% and 8%, respectively. Klaas et al. (2001) publish ISOPHOT measurements for the whole object at 10, 12, 15, 25, 60, 90, 120, 150, 180 and 200 μm and SEST data at 1300 μm. They quote uncertainties of about 5% at 100–150 μm and up to 10%–20% for the other ISOPHOT passbands and for SEST.

Charmandaris et al. (2002) report ISOCAM observations in various mid-IR bands of the interacting system with a spatial resolution of few arcsec, hence resolving the two nuclei. These results are consistent with the photometric observations in the N-band by Mirabel et al. for the southern nucleus, but are systematically fainter for the northern one. Then we split the IRAS and the ISOPHOT long wavelength fluxes between the two nuclei based on the Charmandaris et al. photometry: for $\lambda \leq 12$ μm we assumed a ratio between the IRAS and ISOPHOT fluxes belonging to the two nuclei equal to the ratio between the Charmandaris et al. (2002) ISOCAM 11.4 μm fluxes; while longward 12 μm we adopted the ratio between the fluxes from the two nuclei by Charmandaris et al. (2002) in the ISOCAM 15 μm filter (see Table 2 and Fig. 10).

Since the northern component is very faint compared to the southern one, the uncertainties in method strongly affect the fluxes of the northern nucleus. Therefore, as concerns the

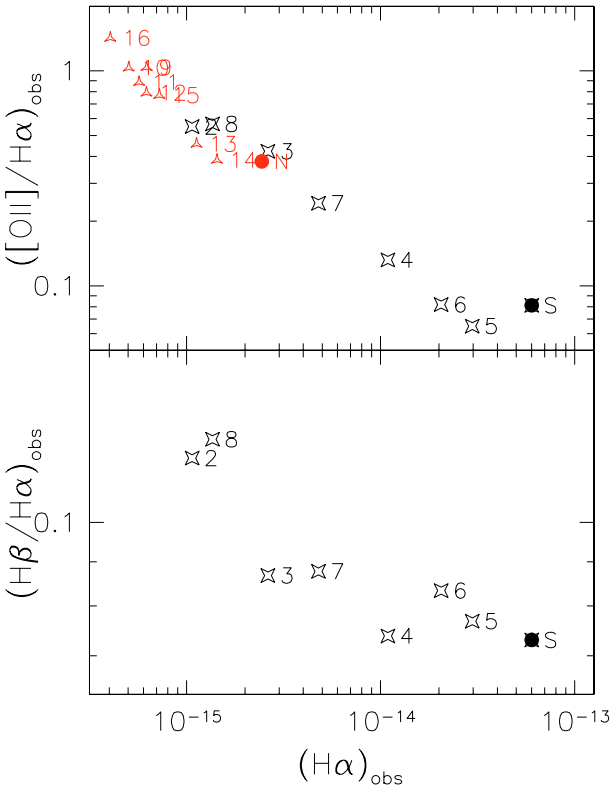

Fig. 7. [OII](3727Å)/Hα and Hβ/Hα flux ratios vs. Hα, before extinction correction. Each data point is labelled according to Fig. 1 (the southern nucleus refers to spectra #4, 5, 6; the northern to #13 and 14). There is a clear dependence of the ratios to the intensity of Hα, suggesting a tight relationship between extinction and Hα luminosity, indicative that the most active (luminous) regions are also the more extinguished. See Fritz et al. (2003) for a detailed discussion.

northern nucleus, we consider fluxes obtained in this way reliable only shortward of 25 μm.

Almost 90% of the infrared flux is emitted within the two 8″ circular regions centered on the nuclei to which the optical photometry is referred, the southern nucleus being responsible for about ~95% of this flux.

4.1. Slit-loss corrections

To match the broad band SED obtained above with the optical spectra measured within our slit, we have modelled the surface brightness profile of Hα with an axially-symmetric bidimensional Gaussian. The free parameters, namely the peak value and the variance σ, were estimated by fitting this profile along the slit with a linear Gaussian as shown in Fig. 8. The values derived are $\sigma_{\rm south} = 2.6$ pixels and $\sigma_{\rm north} = 2.1$ pixels, corresponding to 1.04″ and 0.84″, for the southern and northern nuclei respectively.

The volume under the 3D Gaussian is simply given by the integral of the profile summed to the zero–level flux given by the continuum between the nuclei. To evaluate what fraction of the emitted flux falls outside the slit, we integrated "by slices" within the 1.2″ × 8″ apertures centered on the nuclei. As a result, about the 58% of the light coming from the 8″ aperture centered on the southern nucleus, and about 75% of that

Table 2. Observed fluxes and magnitudes of the Superantennae. Optical and IRAS data, from Mirabel et al. (1991), are in the first thirteen rows, the next six rows report the ISOCAM LW bands fluxes by Charmandaris et al. (2002) and finally Klaas et al. (2001) measurements are in the last eleven rows; the 1300 μm datum was obtained with SEST, while the others with ISOPHOT. Infrared observations marked with * have been splitted between the two nuclei, by means of a procedure described in the text. Integrated IR fluxes were obtained from IRAS data through Sanders & Mirabel (1996) calibration and are expressed in W m^{-2}.

	South 8″	North 8″	Global
B	0.365 mJy	0.324 mJy	1.401 mJy
V	0.880 mJy	0.687 mJy	2.997 mJy
R	1.397 mJy	0.949 mJy	4.220 mJy
I	2.052 mJy	1.407 mJy	6.197 mJy
J	3.544 mJy	2.664 mJy	–
H	5.720 mJy	3.353 mJy	–
K	7.586 mJy	3.467 mJy	–
L	20.79 mJy	2.117 mJy	–
N	110.6 mJy	23.76 mJy	–
S(12 μm)	0.210* Jy	0.012* Jy	0.222 Jy
S(25 μm)	1.217* Jy	0.025* Jy	1.242 Jy
S(60 μm)	5.370* Jy	–	5.484 Jy
S(100 μm)	5.671* Jy	–	5.789 Jy
S(6 μm)	0.0900 Jy	0.0019 Jy	0.0919 Jy
S(6.75 μm)	0.1069 Jy	0.0048 Jy	0.1117 Jy
S(7.75 μm)	0.1501 Jy	0.0083 Jy	0.1584 Jy
S(9.62 μm)	0.0912 Jy	0.0051 Jy	0.0963 Jy
S(11.4 μm)	0.1075 Jy	0.0059 Jy	0.1134 Jy
S(15 μm)	0.2840 Jy	0.0059 Jy	0.2899 Jy
S(10 μm)	0.116* Jy	0.007* Jy	0.123 Jy
S(12 μm)	0.189* Jy	0.011* Jy	0.200 Jy
S(15 μm)	0.392* Jy	0.008* Jy	0.400 Jy
S(25 μm)	1.293* Jy	0.027* Jy	1.320 Jy
S(60 μm)	5.456* Jy	–	5.570 Jy
S(90 μm)	5.153* Jy	–	5.260 Jy
S(120 μm)	4.183* Jy	–	4.270 Jy
S(150 μm)	2.998* Jy	–	3.060 Jy
S(180 μm)	2.253* Jy	–	2.300 Jy
S(200 μm)	1.577* Jy	–	1.610 Jy
S(1300 μm)	0.011* Jy	–	0.012 Jy
$S_{\rm IR}$	5.205×10^{-13}	1.26×10^{-14}	5.28×10^{-13}

coming from the same region around the northern nucleus, were lost by our optical spectroscopic observations.

The next step was to consider the amount of light enclosed in the observed nuclear regions, namely within spectra numbered 4, 5 and 6 for the southern component, and 13, 14 for the northern one. Considering that the observed Hα emission is likely to appear broadened because of the higher extinction in the very inner region of the nucleus, we find that about 50% of the flux observed from a circular aperture of 8″ on the southern object is emitted within this 1.2″×3.6″ aperture corresponding to spectra 4, 5, and 6. Assuming that the far-IR emission mimics the spatial distribution of the Hα line, the ratio $S_{\rm IR}/S_{5550}$ between the bolometric infrared and the *V* band fluxes turn out to be ≃90 for the southern nucleus[1].

[1] The flux at 5550 Å is computed as the mean value within about 50 Å centered at $\lambda = 5550$.

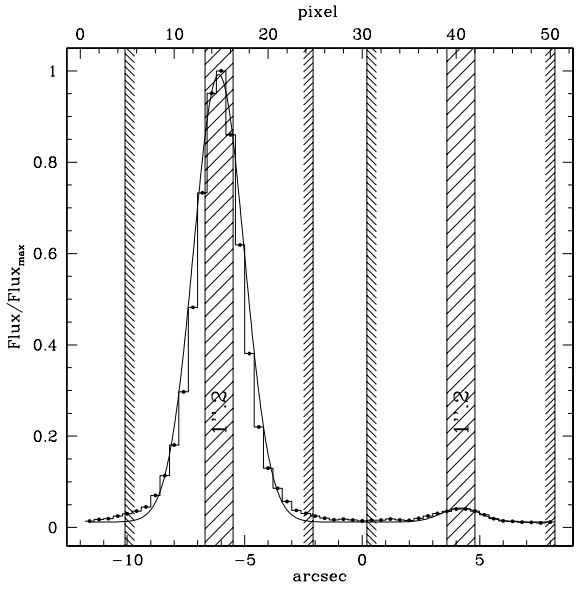

Fig. 8. Spatial profile along the slit, at the wavelength of Hα, used to evaluate the amount of energy encircled within the 8″ aperture centered on each nucleus (delimited with shaded borders), which falls outside the slit (1.2″ shaded regions). After performing a Gaussian fit to the profile, slit losses were estimated assuming that the bidimensional light profile is an axial-simmetric Gaussian.

Similarly we estimate a slit-loss of about 90% from the northern nucleus (1.2″ × 2.4″ aperture for spectra 13 and 14) and, correspondingly, a ratio $S_{\rm IR}/S_{5550} \simeq 9$.

5. The spectral synthesis model

The optical spectrum carries a wealth of information on the recent star formation history and dust extinction. In this section we describe our detailed analysis of the optical spectrum for each separate nuclear component.

As a best approach to describe the irregular star-formation histories of starburst galaxies, we have adopted a completely *free-form* galaxy spectral synthesis model derived as a modofication of that discussed in Poggianti et al. (2001). The optical observed spectrum is modelled as a combination of up to 10 simple stellar populations (SSP) of solar metallicity and different age. Each SSP is meant to represent a formation episode of average constant star formation rate (SFR) over a suitable period Δt (see Table 3).

As the main information provided by the spectrum are the shape of the continuum, (nebular) emission lines and (photospheric) absorption lines, we have chosen 3 classes of SSPs spectra to reproduce these features: young, intermediate and old. The ages of the 10 populations have been chosen by considering the evolutionary timescales of the stars associated with the observational constraints: the youngest generations (10^6, 3×10^6, 8×10^6, 10^7 yr) are responsible for the ionizing photons producing the emission lines an for the UV continuum; intermediate populations (5×10^7, 10^8, 3×10^8, 5×10^8, 10^9 yr) have the strongest Balmer absorption lines; while older generations of stars provide a significant contribution to the spectral continuum, hence affecting also the equivalent widths of the lines. The latters have been modelled with a constant star formation rate (SFR) between 2 and 12 Gyr before the observation.

Each single population is assumed to be extinguished by dust in a uniform screen according to the standard extinction law of the diffuse medium in our Galaxy ($R_V = A_V/E(B-V) = 3.1$, Cardelli et al. 1989). While a more complex picture of the extinction cannot be excluded, Poggianti et al. have already shown that, in the case of obscured starbursts, the characteristics of the emerging spectrum require a significant amount of *foreground* dust (screen model). For a uniform mixture of dust and stars, an increase of the obscuration does not yield a corresponding increase in the *reddening* of the spectrum, and $E(B-V)$ saturates to a value of ∼0.18, too low to account for the observed emission line ratios. In our case the extinction value $E(B-V)$ is allowed to vary from one stellar population to another and the summed extinguished spectral energy distributions of all the single generations make up the total integrated spectrum.

The integrated spectra of the SSPs have been computed with a Salpeter initial mass function (IMF) between 0.15 and 120 $M_\odot$. We have adopted the Pickles (1998) spectral library, after extending its atmospheres with Kurucz (1993) models outside its original range of wavelengths, from 1150 Å to 25 000 Å. The composite (stars+gas) spectra have been obtained through the ionization code CLOUDY (Ferland 1990).

The best-fit model was obtained by minimizing the differences between observed and model selected features: the equivalent widths of five lines ([OII]λ3727, Hδ, Hβ and Hα) and the relative intensities of the continuum flux in a number of almost featureless spectral windows which are chosen according to the spectra charachteristics.

As already anticipated our spectral resolution does not allow to resolve the Hα-[NII] blend. Colina et al. (1991), on high resolution spectra, have found that Hα is about 30% fainter than [NII]6584. Because our spectral synthesis analysis does not model the [NII]6548 line, we apply a correction factor to account for this contribution to the blend.

A critical constraint that we impose to the model is to reproduce the observed infrared to optical flux ratio $S_{\rm IR}/S_{5550}$. Our predicted infrared flux is computed as the difference between the total non-absorbed and the absorbed model spectra.

The minimization procedure applies the algorithm of Adaptive Simulated Annealing (ASA, Ingber 1989, 2000) to a suitable merit function (MF) based on the differences between modelled and observed selected spectral features:

$$F = \sum_{i=1}^{n} \left(\frac{M_i - O_i}{E_i} \cdot W_i \right)^2 \qquad (3)$$

where M_i and O_i are respectively model and observed fluxes (or equivalent width), and E_i and W_i are the corresponding errors and weights. The latter are used to reduce the weight of some observables particularly difficult to model (as the OII line flux).

The minimization procedure checks if any of the SSPs older than 10^7 years contibutes by less than 1% to the total flux at each wavelength. This may happen, for instance,

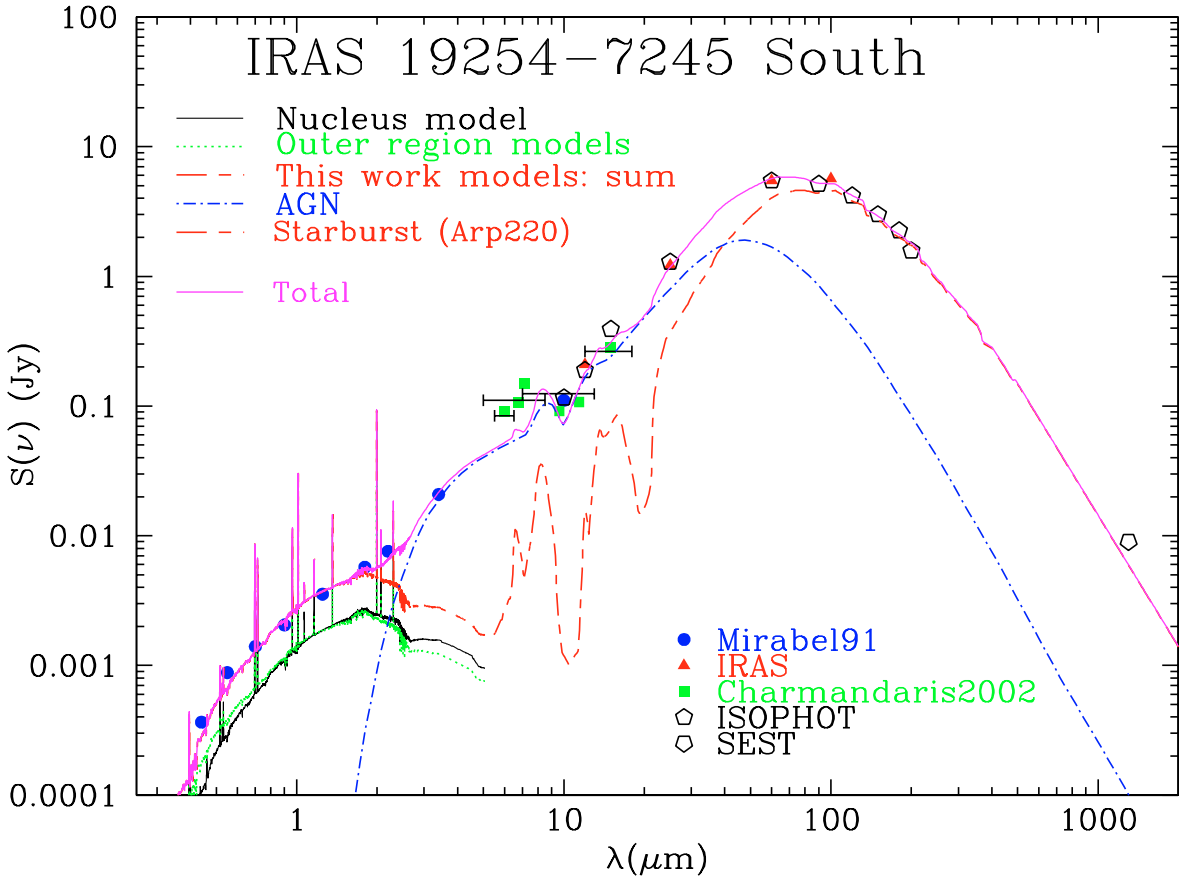

Fig. 9. Spectral energy distribution of the southern nucleus. Data are from Mirabel et al. (1991), Laurent et al. (2000) and Klaas et al. (2001) as described in the text. The thick solid line is the fit to the global SED, obtained combining an optical–NIR fit (dashed line short ward 5 μm) to our spectra (corrected to the 8″ aperture) with an AGN model obtained with the code DUSTY (dot–dashed line) and a semiempirical starburst Arp220–like template (dashed line long ward 5 μm). The thin solid and dotted lines show the fit of the central and outer regions spectra. The *N* band width is slightly shifted upward with respect to the observed datapoint, in order not to be confused with the LW2's.

when extinction becomes too large; in that case that SSP is no more relevant for the fit and is not used. Obviously, the same does not apply to younger SSPs because, though very extincted, their contribution to the FIR emission could not be neglected.

Effectively only few populations dominate the sinthetic resulting spectrum: as can be seen from Table 3, the number of SSP used in the fits decreases to 4 or 5 tipically.

6. The AGN contribution to the broad band spectral energy distribution

The broad band SEDs of the two nuclei of the Superantennae, together with the best-fit optical synthetic spectra are shown in Figs. 9 and 10, respectively.

6.1. The southern nucleus

The resulting SED of the southern nucleus is compared in Fig. 9 with a model obtained from the combination of three different physical components.

In the optical domain, it is the result of our spectral synthesis analysis. The model is obtained combining two different fits, belonging to the central (#4, 5, and 6 – thin solid line in Fig. 9) and outer (#2, 3, 7 and 8 – dotted line) regions spectra, normalized in order to account for the slit losses. The two spectral combinations are used to describe the nuclear and large-scale galactic emissions. Indeed the sum of the two (short–long dashed line) reproduces quite well the optical photometric data, as anticipated in Sect. 2. It is worth noticing that the spectral model reproduces well also the photometric data beyond 7000 Å up to the *H* band.

A first inspection shows that from this fit there remains a strong residual excess in the *K* and *L* bands with respect to the stellar component fitting the optical data. Longwards of the *H* band, the observed fluxes seem to follow a power-law shape, possibly due to the Seyfert II emission, while the stellar spectral component turns down. This excess is even more evident in the *L* band, where the stellar emission is fainter and dust reprocessing of young stellar emission is not yet relevant. The observed $J - L$ colour is about 3.9 mag, while that of the best fit galactic model is $J - L \simeq 2.7$ mag. The latter is consistent with the value observed in the northern nucleus, see Table 2 and Fig. 10, which does not require an AGN contribution.

In order to reproduce this excess we added a QSO template, requiring that the stellar plus AGN component, due to circumnuclear dust, match the *L* band flux. Pernechele et al. (2003) performed a detailed polarimetric analysis of the optical emission of IRAS 19254–7245, revealing a scattered

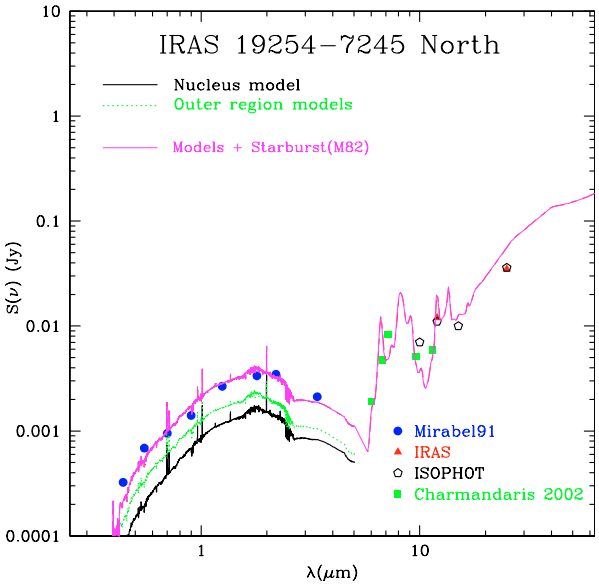

Fig. 10. The spectral energy distribution of the northern nucleus. The fit (thick solid line) is obtained by adding an optical–NIR model short ward 5 μm, and a semiempirical starburst M 82–like template (long ward 5 μm). The thin solid and dotted lines show the fit of the central and outer regions spectra. No AGN component is needed in this case.

polarized component at 2% level only. For this reason we generate a totally obscured AGN model with the code DUSTY (Ivezić et al. 1999) assuming a spherical geometry and a standard ISM. As an alternative, we also checked our fit using the totally obscured edge–on AGN models by Andreani et al. (1999), finding a full consistence with the DUSTY results.

The free parameters for the AGN fit are the ratio R between the inner and outer radii of the spherical dust distribution and the optical depth τ_λ at 0.55 μm.

At wavelengths longer than 10 μm the contribution of the starburst starts to rise again. We thus added an Arp220–like starburst template (short–long dashed line) normalized in order to account for the remaining IR luminosity produced by the southern nucleus. Our template was obtained by merging the GRASIL synthetic model by (Silva et al. 1998) of Arp220 to the CAM–CVF spectrum between 5 and 20 μm by Charmandaris et al. (1999).

We then imposed that the sum of the AGN and starburst templates should reproduce the observed optical-infrared SED. Our best fits for the AGN emission were obtained for R values between 150 and 400, and an absorption $\tau_{0.55\ \mu\mathrm{m}} = 30{-}40$ mag. Adopting higher values of $\tau_{0.55\ \mu\mathrm{m}}$ would underestimate progressively the K band and the L band fluxes, as τ grows, because of self absorption in the AGN dust emission. By converse, lower extinction values would lead to an overestimation of the NIR fluxes.

The parameter R, modelling the size of the circum-nuclear dust distribution around the AGN, has a moderate impact on our global fitting procedure: by increasing R we essentially add cold dust in the outer parts far away from the central AGN, hence slightly increase the AGN emission around 100 μm. However, there is limited variance allowed to this: our best fit shows that with values $R < 150$ or $R > 400$ would completely spoil the fit to the observed SED.

In this way we estimate that the contribution of the AGN to the bolometric IR flux (estimated from IRAS data) ranges between about 40% and 50%.

The resulting model is the thick solid line in Fig. 9; we note that it does not fit the observed 6−7 μm data, possibly characterized by strong PAH features. Actually DUSTY doesn't account for the PAH emission and there could be also some residual PAH from the starburst component, not reproduced by the Arp220 template. On the other hand the cause of this discrepancy could also be the spherical geometry assumption.

This analysis, in turn, suggests that a similar fraction of the Hα emission could originate from the AGN. Indeed Cid Fernandes et al. (2001), analysing the properties of a sample of 35 Seyfert II nuclei, find that it is possible to set some rough constraints on the non–thermal Hβ component from the properties of the [OIII]/Hβ ratio: they show how values of [OIII]/Hβ between 4 and 13 imply an AGN contribution to Hβ between 30 and 100%. On this basis, the measured IRAS19254 South [OIII]/Hβ of ∼6 leads to a non–thermal contribution of ∼40% to the Hβ emission, consistent with our estimate in the infrared.

In the followings we will thus assume that about 40% of the line emission is due to the AGN.

6.2. The northern nucleus

As far as the northern nucleus is concerned, we found essentially no evidence for an AGN component. The observed data consist in the set of optical and near–IR observations by Mirabel et al. (1991), the mid–IR ISOCAM fluxes by Charmandaris et al. (2001) and the IRAS and ISOPHOT fluxes up to 25 μm, obtained splitting literature data for the whole (North + South) Superantennae through the method described in Sect. 4. The latters are obviously more uncertain, but are still consistent with Charmandaris et al. (2001) data, which are affected by a ∼10−20% uncertainty.

The fit is obtained by means of a pure stellar component, modelled as in Sect. 5, from the optical to the NIR, and a starburst component based on the prototype M82, at $\lambda > 5$ μm. The latter is obtained by merging a synthetic SED modelled with Silva et al. (1998), with the observed CVF spectrum by Schreiber et al. (2001) between 5 and 18 μm.

The best fit is shown in Fig. 10. A small excess still present in the L band may be due to PAH 3.3 μm emission not included in our spectral model.

7. Results of the spectral analysis

In this Section we discuss our results for the two nuclei separately and then we extend our analysis to the outer regions of the galaxy.

The merit function (Eq. (3)) has been built on 10 continuum bands (3550–3670 Å, 3890–4020 Å, 4140–4300 Å, 4400–4500 Å, 4700–4820 Å, 5080–5180 Å, 5360–5660 Å, 5950–6110 Å, 6880–6980 Å and 7750–8500 Å), and 5 spectral lines, Hα+[NII], Hβ and [OII]3727, Hδ and Hγ. The latter

Table 3. Spatial dependence of the star formation rate ($M_\odot$/yr) and extinction (A_V) in Superantennae, as derived from the best fit models. Each row refers to a different SSP; ages and durations, in years, are reported in columns two and three respectively. The following pairs of columns refers to the numbered galaxy regions and provide the SFR and extinction values for each SSP. Values are not shown when the star formation rate is negligible. The bottom three rows in each panel give the total stellar mass sampled by the spectrum and the A_V extinction as computed combining the three youngest populations (young) and all the 10 SSPs (total). See text for more details.

SSP			Spectra											
#	Age	Δt	2		3		Nucleus S		7		8		9	
			SFR	A_V	SFR	A_V	SFR	A_V	SFR	A_V	SFR	A_V	SFR	A_V
1	10^6	2×10^6	0.09	–	12.14	5.27	77.85	15.25	3.07	4.86	0.43	1.37	0.09	0.25
2	3×10^6	4×10^6	0.21	2.27	0.10	–	62.28	3.62	1.89	2.04	0.02	–	0.05	2.28
3	8×10^6	3×10^6	–	–	–	–	–	–	–	–	–	–	–	–
4	10^7	4×10^6	–	–	–	–	–	–	–	–	–	–	–	–
5	5×10^7	6.2×10^7	–	–	–	–	–	–	–	–	–	–	–	–
6	10^8	1.25×10^8	–	–	–	–	–	–	1.32	2.04	–	–	–	–
7	3×10^8	2×10^8	0.17	1.50	0.25	1.35	–	–	–	–	–	–	–	–
8	5×10^8	3.5×10^8	2.30	1.15	2.18	1.35	6.58	2.31	1.05	1.52	2.26	1.52	–	–
9	10^9	1.25×10^9	–	–	–	–	14.48	1.73	–	–	–	–	1.45	1.46
10	1.2×10^{10}	10^{10}	0.49	1.03	0.97	1.18	3.89	0.79	1.72	1.52	1.15	1.43	0.33	0.75
$M_{\rm tot}$			5.69e9		1.05e10		5.97e10		1.77e10		1.23e10		5.12e9	
A_V(young)			1.741		3.390		3.838		2.305		0.905		1.252	
A_V(tot)			1.169		1.530		2.278		1.668		1.437		1.216	

			10		11		12		Nucleus N		15		16	
			SFR	A_V	SFR	A_V	SFR	A_V	SFR	A_V	SFR	A_V	SFR	A_V
1	10^6	2×10^6	0.12	1.11	0.13	0.73	0.25	1.25	0.50	0.47	0.42	1.48	0.06	–
2	3×10^6	4×10^6	0.03	1.11	–	–	–	–	0.26	3.18	–	–	0.08	3.45
3	8×10^6	3×10^6	–	–	–	–	–	–	–	–	–	–	–	–
4	10^7	4×10^6	–	–	–	–	–	–	–	–	–	–	–	–
5	5×10^7	6.2×10^7	–	–	–	–	–	–	–	–	–	–	–	–
6	10^8	1.25×10^8	–	–	–	–	–	–	–	–	–	–	–	–
7	3×10^8	2×10^8	–	–	–	–	–	–	–	–	–	–	–	–
8	5×10^8	3.5×10^8	–	–	–	–	0.17	1.25	23.5	2.10	9.07	1.78	0.62	0.40
9	10^9	1.25×10^9	0.50	1.11	0.36	0.73	1.94	1.25	–	–	–	–	0.92	0.15
10	1.2×10^{10}	10^{10}	0.52	0.70	0.52	0.73	0.14	1.25	2.70	0.37	0.22	0.40	–	–
$M_{\rm tot}$			5.84e9		5.631e9		3.91e9		3.52e10		5.37e9		1.39e9	
A_V(young)			1.101		0.721		1.233		1.606		1.467		1.865	
A_V(tot)			0.826		0.721		1.233		1.633		1.572		0.639	

two lines were assigned a weight of 0.3 because they are too faint and, in the case of Hγ, because of contamination by [OIII]4363, which is not considered in our models.

We required that the model should reproduce the ratio $S_{\rm IR}/S_{5550}$ between the far-infrared and the optical flux, as defined in Sect. 4 and aperture corrected according to Sect. 4.1. The FIR flux was corrected for the contribution of the AGN, assumed to amount to 40% of the bolometric IR emission (see Sect. 6).

The errors in the continuum flux were computed according to the local signal to noise ratio, while in the case of the lines fluxes the relative errors were assumed proportional to $1/\sqrt{I_\lambda}$, where I_λ is the flux emitted by the corresponding line.

Table 3 summarizes the parameters leading to the best fits: for each spectrum SFR and A_V of the populations which build the sinthetic model are reported. Basically only 4 or 5 SSPs significantly contribute to the emitted spectra, therefore decreasing to 8 or 10 the number of parameters used to fit the 16 observed features chosen.

7.1. Models for the southern nucleus

The spectrum of the southern nucleus is obtained by summing the spectra with the strongest continuum and emission lines, namely those labelled with numbers 4, 5 and 6 (see Fig. 1).

Our best-fit solution is illustrated in Fig. 11. The upper panel shows the observed and model spectrum (both normalized at 5500 Å) and their differences, the lower panel reports the contribution of the dominant stellar populations. All the modelled features are within 1σ error from their observed values, except for the [OII] line (3σ) and for the band around 4760 Å. Figure 12 illustrates the star-formation history and extinction distribution of the best-fit model. The optical spectrum is mainly contributed by an old population (about 12 Gyr), providing about 65% of the total luminous mass, and an intermediate one (about 5×10^8–10^9 yr) forming about 35% of the total luminous mass. On top of this there is the contribution of a strong and heavily extinguished burst of star formation, which account for the strong observed emission lines and for the intense FIR flux (see Fig. 11), but give

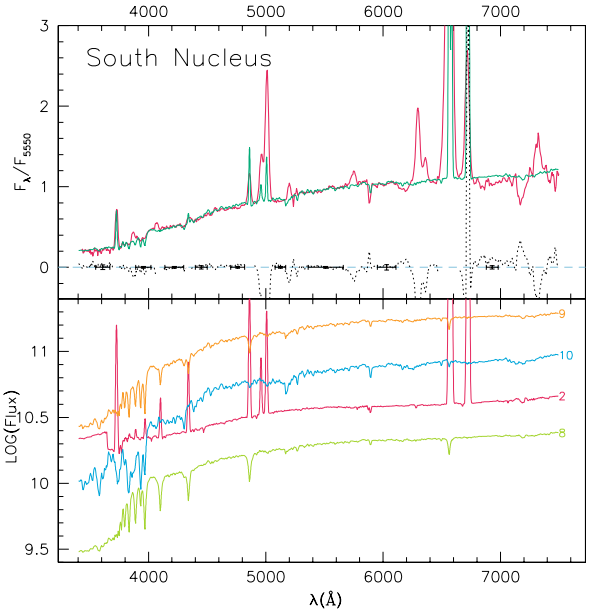

Fig. 11. Best fit model for the southern nucleus. Top panel reports the observed (thick line) and the model (thin line) spectrum, the dotted line shows the residuals between model and observed spectra. Bottom panel depicts the contribution of each extinguished SSP (labeled from 1 to 10 with increasing age). The intermediate age population dominates the continuum luminosity, while the 2–6 Myr population provides the emission lines.

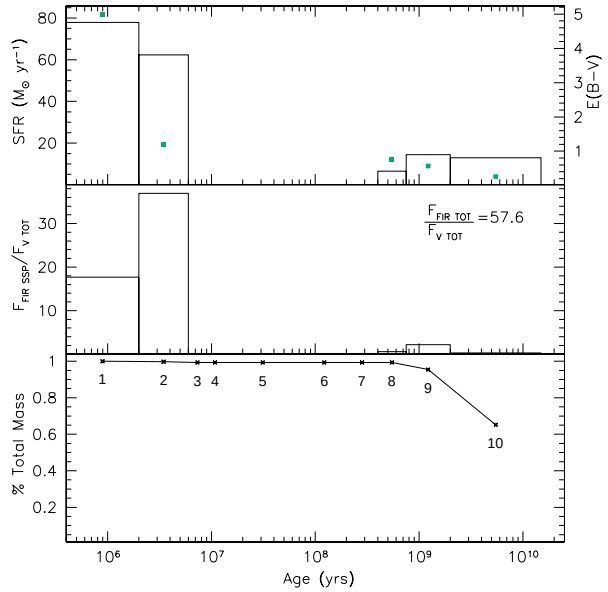

Fig. 12. SFR and extinction of the southern best fit model. Top panel: SFR (histogram and left scale) and colour excess (filled squares and right scale) for the different stellar populations. Middle panel: ratio between the bolometric FIR emission due to each SSP and the total V band flux. Notice that the sum over all populations is not 100, but turns out to be 57.6, which is the ratio between the *total* FIR and V fluxes. This number is the conversion factor to obtain the differential contribution of each SSPs to the integrated infrared light. Bottom panel: cumulative mass formed in the galaxy: about 35% of the total stellar mass has been processed by the intermediate age star formation episode, 60% belongs to the oldest. The youngest stars, significantly contributing to the FIR bolometric emission and dominating the lines fluxes, provide almost no contribution to the total luminous mass formed in the galaxy.

a negligible contribution to the total luminous mass. The extinction shows the characteristic age-selective pattern in which the youngest populations are more heavily obscured than the older ones. In this case the youngest population is completely obscured with an $E(B-V) \simeq 5$ and cannot be seen in the optical spectrum. The old populations with age $\geq 10^9$ yrs have $E(B-V) < 0.5$.

In order to test the possibility of an alternative star formation history, characterized by a much longer starburst duration, we tried a constant star formation rate over the last 5×10^8 years. The corresponding star formation and extinction patterns are shown in Fig. 13: with this constraint, the code attempts to minimize the impact of the intermediate age SSPs by increasing their extinction. The predicted IR flux is within 3σ from the observed value, and there are only little differences with respect to the best-fit model in the optical spectrum. Although this solution cannot be formally excluded a priori, we consider it very unlikely, since extinction values so much higher for all the intermediate age compared with the youngest populations do not have any physical meaning.

7.2. Models for the northern nucleus

The spectrum of the northern nucleus (spectral regions #13 and 14) was analyzed with the same fitting procedure described previously. The results are shown in Figs. 14 and 15: the star formation history of this nucleus closely resembles that of the southern one, with two main star formation episodes and a recent, much weaker, burst. The extinction appears to be lower than that of the southern nucleus.

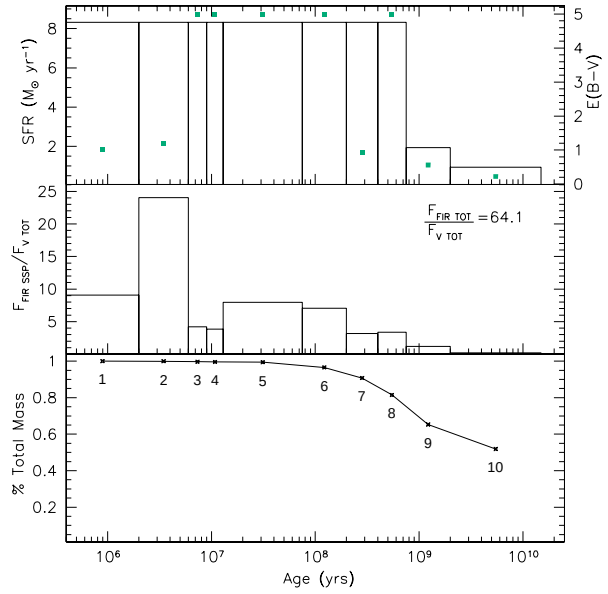

Fig. 13. A good fit to the optical spectrum of the southern nucleus (not shown here) is found even by imposing a constant long burst of star formation. However the fitting procedure "obscures" unnecessary populations, which only contribute to the FIR. Due to this behaviour of the color excess we exclude such a star formation scenario.

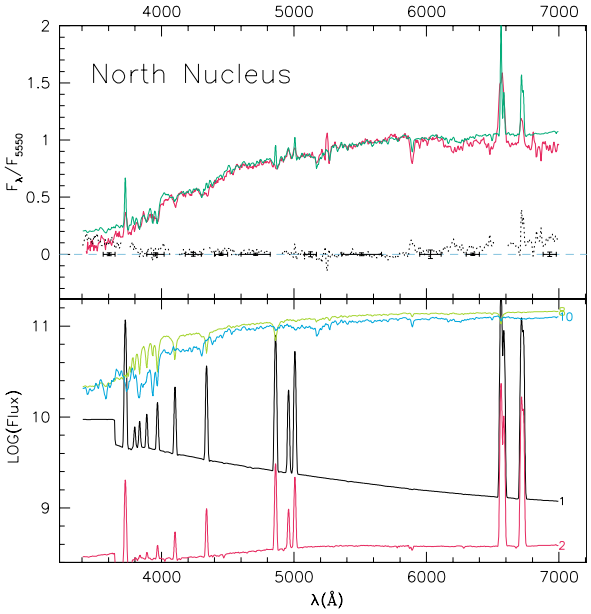

Fig. 14. Best fit to the northern nucleus spectrum. The mismatch at the edges of the spectral range analysed is found in all other models we have tried.

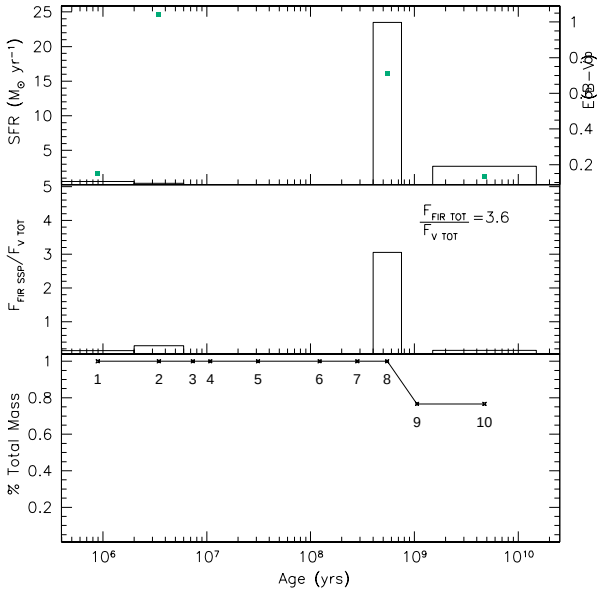

Fig. 15. SFR and colour excess of the northern nucleus best fit model. The star formation history of this nucleus closely resembles that of the southern nucleus, with two main star formation episodes, forming 75% and 25% of the total stellar mass respectively. The intermediate age population provides the bulk of the FIR flux. Extinction is significately lower than in the southern nucleus.

The old population contributes up to 75% in mass and the intermediate age population (0.5 Gyr) about 25%.

Note that there are problems in fitting the observed continuum in the range 6000 Å to 7000 Å, which we were not able to solve, even adopting different extinction laws, SSP metallicity, or different SSP combinations. A similar problem is found between 3400 and 3800 Å, where the model systematically overestimates the observed spectrum, but here the observed spectrum has a low S/N ratio.

7.3. Models for the regions outside the nuclei

We have obtained best-fit models for the spectra of all the individual regions along the line connecting the two nuclei. Here both the continuum and line intensities are much lower than those from the two main nuclei (Fig. 5), and the star formation activity correspondingly low (see Table 3). Nevertheless the main characteristic of the star formation history of the two nuclei, namely the evidence for an old stellar population and for two main episodes of SF, one at $\sim 10^9$ yrs and one ongoing, seems also reflected in the spectra of the extranuclear regions.

8. Discussion

We discuss here our previous results on the star formation history, extinction properties, and the AGN contribution in the *Superantennae*.

8.1. Spatial-dependent star formation and extinction in Superantennae

Table 3 reports our modelled values of the average star formation rate ($M_\odot$/yr) along the slit for stellar populations at different ages. This quantity has been derived from the total stellar mass of the population of a given age divided by the duration Δt of the SF episod (third column in the table). We have then computed the total stellar mass, sampled along the slit, and the corresponding visual extinction for the various populations.

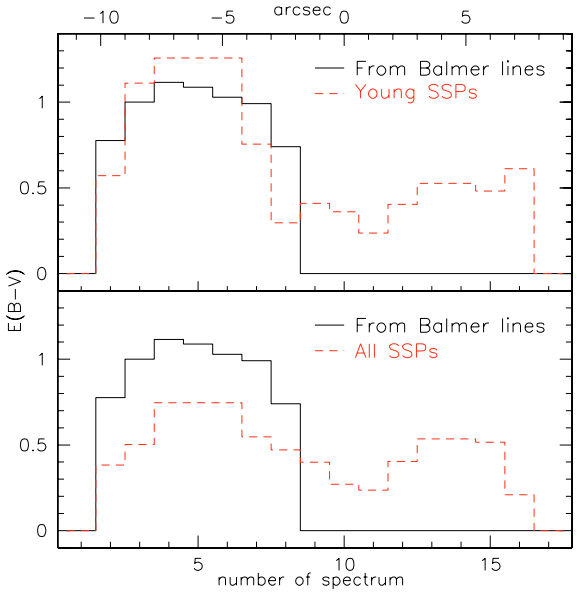

Fig. 16. The spatial dependence of the extinction, as computed on the basis of the Balmer decrement and through the spectrophotometric modelling of the spectra (see Table 3). The Balmer decrement has not been applied in regions 9 to 17 where Hβ is not detected or appears in absorption.

Figure 16 compares the $E(B-V)$ values obtained with our global fitting procedure with those derived from the Balmer decrement, after correcting Hβ for stellar absorption. In the

upper panel we show the $E(B-V)$ distribution obtained combining the three youngest SSPs, while in the lower panel that derived averaging over all ten stellar populations. In the latter case the Balmer decrement technique appears to sistematically overestimate the extinction, while in the former there is a better agreement at least close to the southern nucleus. This is because of the different extinction properties of various populations, which the global fitting model can deal with, but not the integrated spectrum. Also, by accounting for the contributions of the intermediate age stars, the model provides a fair estimate of the reddening even in those regions where Hβ is in absorption and the Balmer decrement technique is inapplicable (e.g. spectra from 9 to 17).

Table 4 compares the *ongoing* SFR values obtained from our global fitting procedure (combining the two youngest SSPs) with those derived by Kennicutt (1998) calibrations:

$$\begin{aligned} SFR\left([\mathrm{OII}]\right) &= 1.4\times10^{-41}\times L\left([\mathrm{OII}]\right) M_\odot\cdot\mathrm{yr}^{-1} \\ SFR\,(\mathrm{FIR}) &= 4.5\times10^{-44}\times L\,(\mathrm{FIR})\, M_\odot\cdot\mathrm{yr}^{-1} \end{aligned} \quad (4)$$

and Eq. (2). Before computing the SFR, all the measured fluxes were corrected for internal absorption using the extinction values found in Sect. 3. A value of $E(B-V)=0.4$, based on the results of the spectral synthesis, was assigned to those spectra for which Hβ is not detected or is found to be in absorption (see Sect. 3.1.2). These relations refer to a Salpeter IMF between 0.1 $M_\odot$ and 100 $M_\odot$, while the IMF limits in our code are 0.15 and 120 $M_\odot$: the factor between the two is $\int_{0.1}^{100} m^{-1.35}\mathrm{d}m / \int_{0.15}^{120} m^{-1.35}\mathrm{d}m \simeq 1.162$. The model's SFR of the southern nucleus exceeds by about 20% the SFR estimate based on the FIR flux, but this is within the uncertainties of the calibrations if we considere that Eq. (4) refers to an average continuous SFR over the last 100 Myr, while the best-fit model in Fig. 12 assumes a very young short burst: the latter needs a higher SFR to supply a given FIR luminosity.

The [OII]λ3727 diagnostics leads to a higher SFR than the Hα, with a larger discrepancy in the circumnuclear regions. The [OII]λ3727 line has however a very different spatial profile from [OIII]λ5007, Hα or Hβ (see Fig. 5), indicating a different degree of ionization, possibly due to a metallicity gradient (see Fritz et al. 2002 for a detailed discussion). Moreover the SFR obtained by the [OII]λ3727 line has a large intrinsic uncertainty (Charlot & Longhetti 2001). A fraction of the star formation in the southern nucleus and in the circumnuclear regions is apparently hidden (SFR from Hα is smaller than SFR from FIR even corrected for the AGN contribution), i.e. is not recoverable from the optical spectrum.

Concerning the northern nucleus, the estimates based on the line fluxes and on the spectrophotometric synthesis model analysis agree fairly well. Apparently this region of the galaxy is likely in a post star-burst phase, as suggested by the virtual absence of a very young component. In this case, a substantial discrepancy between the SFR value based on the FIR flux and those based on the other methods is apparent. Figure 15 indicates that the FIR emission of the northern nucleus is produced mainly by a 5×10^8 years old population; therefore applying the SFR calibration based on FIR leads to a misleading estimate, while our modelled SFR value appropriately accounts for the ongoing star-formation activity. Because the youngest populations are those producing nebular emission lines, the Hα and [OII] diagnostics are in much better agreement with our modellistic value.

Table 4. Values of the ongoing star formation rate SFR (in $M_\odot$/yr) derived from: the main emission lines, after correction for extinction and for the AGN contribution, and adopting the the Kennicutt's calibration; from the far-IR luminosity (Kennicutt's calibration); and from our global best-fit model. The latter has been computed combining the two youngest single stellar populations. All SFRs dignostics adopt a Salpeter IMF between 0.1 and 100 $M_\odot$.

Spectrum	Hα	[OII]	FIR	Model
1	–	–	–	–
2	0.22	0.59	0.25	0.21
3	1.04	4.23	2.94	4.78
South	46.60	74.67	66.02	78.40
7	2.28	6.79	2.94	2.65
8	0.29	0.85	0.25	0.19
9	–	–	–	0.07
10	–	–	–	0.07
11	0.11*	0.13*	–	0.05
12	0.12*	0.13*	–	0.09
North	0.48*	0.29*	1.32	0.40
15	0.14*	0.15*	–	0.16
16	0.08*	0.15*	–	0.08
17	0.08*	0.14*	–	–

*: Values obtained assuming $E(B-V)=0.4$ in these regions of the galaxy.

Concerning the past star formation history, we find evidence for two distinct episodes in this merging system. A recent, still ongoing burst producing the optical emission lines and the strong infrared flux, and an older one which took place about 1 Gyr ago. Remarkably enough, this double–peaked recent star formation history appears to be common to all the regions within our aperture. Analysing a sample of interacting Ultraluminous IR Galaxies, Murphy et al. (2001) suggest that the merging events may evolve through various steps corresponding to different encounters, hence ULIRGs may show evidence for multimodal stellar generations. Colina et al. (1991) give an estimate of about 1 Gyr for the age of the first encounter, based on the extent and the speed of the gas in the tails of the system. Our results are fully consistent with this overall picture of the merging process, and relate the two main episodes of activity with the first encounter and the final merging of the two galaxies. In this context, Fig. 15 suggest that at the time of the second enounter the gas in the northern nucleus was already almost exhausted. During the first encounter about 30% of the total stellar mass was formed, while the remaining 70% had already been formed by a pre-existing older generation of stars.

Our model gives very similar masses for the two nuclei, consistent with the analysis of Colina et al. (1991) who, based

on dynamical considerations, infer a ratio ∼1 between the masses of the two progenitor galaxies.

8.2. The contribution of the AGN

Our analysis of the optical-FIR SED has found evidence for a substantial type-2 AGN component in the southern nucleus. We have shown, in particular, that the $J-L$ colour may be exploited as an estimator of the AGN contribution to the MID and FIR emission. For example, while the northern nucleus has $J-L \simeq 2.7$ value entirely consistent with a galaxy model dominated by evolved stellar populations, the southern nucleus shows an excess in the L band, $J-L \simeq 3.9$ mag, that unequivocally proves the presence of an AGN. Fitting the global SED with a combination of an AGN and starburst templates, the contribution of the AGN has been constrained to be 40%−50% of the bolometric flux between 8 and 1000 μm. The uncertainty in this estimate is mostly due to uncertainties in the parameter R setting the scale size of the circum-nuclear dust distribution, which affects the dust temperature distribution.

The optical spectrum also indicates the presence of a Seyfert-2 nucleus. Pernechele et al. (2003) provide evidence for ≃2% scattered polarized light around Hα in the southern nucleus. Also the analysis of the [OIII]/Hβ ratio indicates a non–thermal contribution of ∼40% at Hβ, consistent with that required by the MID IR excess.

In X-rays, Pappa et al. (2000) showed that *Superantennae* is characterized by a very hard 2−10 keV spectrum with $L_X \simeq 2\times10^{42}$ erg/s, and Braito et al. (2002) found evidence for a high-equivalent width FeI Kα line typical of heavily obscured type-2 AGNs.

At radio wavelengths, the contribution of the AGN may be evaluated by comparing the observed flux with that expected from a starburst galaxy on the basis of the FIR/radio correlation (e.g. Sanders & Mirabel 1996):

$$q = \log \frac{F_{\rm FIR}/\left(3.75\times10^{12}\ {\rm Hz}\right)}{S_\nu(1.49\ {\rm GHz})/\left({\rm W\ m^{-2}\ Hz^{-1}}\right)} \simeq 2.35 \pm 0.15, \qquad (5)$$

where $F_{\rm FIR} = 1.26\times10^{-14}\ (2.58\,S_{60\,\mu{\rm m}}[{\rm Jy}] + S_{100\,\mu{\rm m}}[{\rm Jy}])$ W m^{-2}. Wright et al. (1994) report a radio emission of $S_\nu \simeq 102$ mJy at 4.85 GHz. Assuming a radio slope $\alpha_R = 0.8$, typical of starforming galaxies, the ratio in Eq. (5) becomes $q \simeq 2.71$. We find instead from Table 2 $q_{4.85\,{\rm GHz}} \simeq 1.83$, significantly lower than the expected value for a normal starforming galaxy. Conversely, assuming that the starburst is responsible of ∼60% of the total infrared flux from Superantennae, and from Eq. (5), we expect for a pure starburst component a 4.85 GHz flux of 7.8 mJy, more than one order of magnitude fainter than observed. So the AGN dominates the radio emission.

Finally, the two merging/interacting systems appear to have almost the same stellar mass (≃6×10^{10} $M_\odot$ and ≃3.4×10^{10} $M_\odot$). From the correlation of the central Massive Dark Object (MDO) mass in galaxy nuclei with the bulge mass (Magorrian et al. 1998), we would then expect that the two nuclei host similar-mass MDO's. The fact that only the southern nucleus is site of AGN activity is consistent with our discussed evidence that the northern nucleus has underwent a past activity episode (possibly involving both a starburst and an AGN), whose feedback and/or gas exhaustion have possibly quenched out any subsequent activity.

9. Conclusions

We have presented a spatially–resolved study of the star formation and extinction properties of the Ultra Luminous InfraRed Galaxy IRAS 19254–7245 (The Superantennae) along the line connecting the two nuclei.

We have combined new optical spectroscopic observations with detailed broad band spectral energy distributions built from published photometry. We have first attempted to quantify the presence of an obscured AGN – for which there are evidences from both X-ray, optical and radio observations – and its contribution to the source spectrum: we have found that the $J-L$ colour may be a powerful diagnostic tool. By means of an elaborate fit of the whole SEDs, from the optical to the FIR, we have inferred that about 40–50% of the luminosity of the southern nucleus in the infrared is due to an obscured AGN. The northern nucleus instead does not show any evidence of an AGN.

After having accounted for the AGN contribution, the combination of the optical spectral data with infrared observations allows to disentangle between extinction, age and star-formation effects: our spatially- and temporally-resolved analysis is able to largely resolve all the degeneracies otherwise present in the integrated spectra. The data on Superantennae are consistent with a recent bimodal star formation history. The first episode of stellar formation possibly corresponds to a first collision between the two progenitor galaxies, about 1 Gyr ago, when a significant fraction of the gas mass was converted in stars (about 30% of the present total mass of the system). The merging onto the current configuration is due to a more recent episode, adding a negligible fraction (few %) of the total stellar mass.

We show that the northern nucleus has been characterized in the past by a slightly older and less intense burst of star formation.

The radio emission by *Superantennae*, which is more than one order of magnitude larger than expected from the starburst if we use the FIR/radio correlation, confirms the presence of an AGN. Having said that, the radio flux cannot be used to estimate the AGN contribution to the bolometric emission. Our analysis also emphasizes that the technique used to estimate the redshift for dusty starbursts and based on the radio to mm flux ratio may provide highly unreliable results if even a minor AGN component is present in the system.

Acknowledgements. We are grateful to G.L. Granato for providing us with models of SED of AGNs and to V. Braito for helpful discussions. AB acknowledges support from the Italian Ministry for University and Research (MURST) under grant Cofin 92001021149-002.

References

Andreani, P., Franceschini, A., & Granato, G. 1999, MNRAS, 306, 161

Barger, A. J., Cowie, L. L., & Richards, E. A. 2000, AJ, 119, 2092

Braito, V., Franceschini, A., Della Ceca, R., et al. 2002, An XMM-Newton Survey of Ultra-Luminous Infrared Galaxies, in Proc. Symp., New Visions of the X-ray Universe in the XMM-Newton and Chandra Era, 26–30 November 2001, ESTEC, The Netherlands [astro-ph/0202352]

Cardelli, J. A., Clayton, G. C., & Mathis, J. S. 1989, ApJ, 345, 245

Charlot, S., & Longhetti, M. 2001, MNRAS, 323, 887

Charmandaris, V., Laurent, O., Mirabel, I. F., et al. 1999, Ap&SS, 266, 99

Charmandaris, V., Laurent, O., Le Floc'h, E., et al. 2002 [astro-ph/0206150]

Cid Fernandes, R., Heckman, T., Schmitt, H., Delgado, R. M. G., & Storchi-Bergmann, T. 2001, ApJ, 558, 81

Colina, L., Lipari, S., & Macchetto, F. 1991, ApJ, 379, 113

Elbaz, D., Cesarsky, C. J., Fadda, D., et al. 1999, A&A, 351, L37

Ferland, G. J. 1996, Hazy, a Brief Introduction to CLOUDY, in University of Kentucky, Departmnt of Physics and Astronomy Internal Report

Franceschini, A., Aussel, H., Cesarsky, C. J., Elbaz, D., & Fadda, D. 2001, A&A, 378, 1

Fritz, J., Berta, S., Pernechele, C., Bressan, A., & Franceschini, A. 2003, in preparation

Genzel, R., Lutz, D., Sturm, E., et al. 1998, ApJ, 498, 579

González Delgado, R. M., Leitherer, C., & Heckman, T. M. 1999, ApJS, 125, 489

Hauser, M. G., Arendt, R. G., Kelsall, T., et al. 1998, ApJ, 508, 25

Hopkins, A. M., Connolly, A. J., Haarsma, D. B., & Cram, L. E. 2001, AJ, 122, 288

Kennicutt, R. C. 1998, ARA&A, 36, 189

Klaas, U., et al. 2001 [astro-ph/0110213]

Kurucz, R. 1993, ATLAS9 Stellar Atmosphere Programs and 2 km/s grid. Kurucz CD-ROM No. 13. Cambridge, Mass.: Smithsonian Astrophysical Observatory

Ingber, L. 1989, Mathematical Computer Modelling, 12, 967

Ingber, L. 2000, Adaptive Simulated Annealing

Ivezić, Ž., Nenkova, M., & Elitzur, M. 1999, User Manual for DUSTY, Univ. Kentucky Internal Rep.

Laurent, O., Mirabel, I. F., Charmandaris, V., et al. 2000, A&A, 359, 887

Magorrian, J., Tremaine, S., Richstone, D., et al. 1998, AJ, 115, 2285

Merritt, D., & Ferrarese, L. 2001, MNRAS, 320, L30

Mirabel, I. F., Lutz, D., & Maza, J. 1991, A&A, 243, 367

Murphy, T. W., Soifer, B. T., Matthews, K., & Armus, L. 2001, ApJ, 559, 201

Oke, J. B. 1990, AJ, 99, 1621

Osterbrock, D. E. 1989, Astrophysics of Gaseous Nebulae an Active Galactic Nuclei, University Science Books, Mill Valley, California

Pappa, A., Georgantopoulos, I., & Stewart, G. C. 2000, MNRAS, 314, 589

Pernechele, C., Berta, S., Marconi, A., et al. 2003, MNRAS, 338, L13

Pickles, A. J., PASP, 110, 863

Poggianti, M. B., Bressan, A., & Franceschini, A. 2001, ApJ, 550, 195

Puget, J.-L., Abergel, A., Bernard, J.-P., et al. 1996, AAP, 308, L5

Sanders, D. B., & Mirabel, I. F. 1996, ARA&A, 34, 749

Schlegel, D. J., Finkbeiner, D. P., & Davis, M. 1998, ApJ, 500, 525

Foerster Schreiber, N. M., Genzel, R., Lutz, D., Kunze, D., & Sternberg, A. 2001, ApJ, 552, 544

Silva, L., Granato, G. L., Bressan, A., & Danese, L. 1998, ApJ, 509, 103

Smail, I., Ivison, R. J., Owen, F. N., Blain, A. W., & Kneib, J.-P. 2000, ApJ, 528, 612

Soifer, B. T., Sanders, D. B., Neugebauer, G., et al. 1986, ApJ, 303, L41

Soifer, B. T., Neugebauer, G., Matthews, K., et al. 2000, AJ, 119, 509

Strauss, M. A., Huchra, J. P., Davis, M., et al. 1992, ApJS, 83, 29

Sullivan, M., Mobasher, B., Chan, B., et al. 2001, ApJ, 558, 72

Vanzi, L., Bagnulo, S., Le Floc'h, E., et al. 2002, A&A, 386, 464

Wright, A. E., Griffith, M. R., Burke, B. F., & Ekers, R. D. 1994, ApJS, 91, 111